

Optically addressable universal holonomic quantum gates on diamond spins

Yuhei Sekiguchi

Yokohama National University

Kazuki Matsushita

Yokohama National University

Yoshiki Kawasaki

Yokohama National University

Hideo Kosaka (✉ kosaka-hideo-yp@ynu.ac.jp)

Yokohama National University <https://orcid.org/0000-0002-3778-7236>

Article

Keywords:

Posted Date: April 8th, 2022

DOI: <https://doi.org/10.21203/rs.3.rs-1461563/v1>

License:   This work is licensed under a Creative Commons Attribution 4.0 International License.

[Read Full License](#)

Version of Record: A version of this preprint was published at Nature Photonics on July 28th, 2022. See the published version at <https://doi.org/10.1038/s41566-022-01038-3>.

Optically addressable universal holonomic quantum gates on diamond spins

Yuhei Sekiguchi¹, Kazuki Matsushita², Yoshiki Kawasaki², and Hideo Kosaka^{1,2*}

¹Institute of Advanced Sciences, Yokohama National University, 79-5 Tokiwadai, Hodogaya, Yokohama 240-8501,
Japan

²Department of Physics, Graduate School of Engineering Science, Yokohama National University, 79-5 Tokiwadai,
Hodogaya, Yokohama 240-8501, Japan

*kosaka-hideo-yp@ynu.ac.jp

Abstract

The ability to individually control the numerous spins in a solid solid-state crystal is essential technology for the development of large-scale quantum processors and memories. Localized laser field offers spatial selectivity for electron spin manipulation through spin-orbit coupling. However, it has been difficult to simultaneously achieve the precise and universal manipulation by itself. Here, we demonstrate microwave-driven holonomic quantum gates on an optically selected electron spin in a nitrogen-vacancy (NV) center in diamond. The electron spin is precisely manipulated with global microwave tuned to the frequency shift induced by the local optical Stark effect. We show the universality of the operations, including state initialization, preparation, readout, and echo. We also generate optically addressable entanglement between the electron and adjacent nitrogen nuclear spin, thus satisfying the scalability requirement of qubits. High fidelity operations are achieved by applying amplitude-alternating pulses, which are tolerant to fluctuations in microwave intensity and detuning. These techniques enable site-selective quantum teleportation transfer from a photon to a nuclear spin memory, paving the way for the realization of distributed quantum computers and the quantum Internet with large-scale quantum storages.

Main text

I. Introduction

Individual spins in solid-state material are promising candidates for quantum memories in large-scale quantum storage, since their weak interaction with the environment realizes their long coherence time¹⁻⁶. However, it is difficult to apply microwaves, which are typically used for spin control, locally on the order of sub microns due to their long wavelength,

making it challenging to selectively manipulate the individual spins. Several techniques have been developed to manipulate the individual spins resonant to a frequency that is spatially non-uniform owing to a gradient magnetic field⁷⁻⁹ or their own random quantization axes determined by the crystal axes^{10,11}. On the other hand, all-optical techniques¹²⁻¹⁸ for spin manipulation via spin-orbit coupling have also been developed to increase the spatial resolution into the diffraction limit. Especially, an optical Stark effect^{19,20} (or stimulated Raman²¹) and geometric phase gate²²⁻²⁷ on color centers in diamond and quantum dots in semiconductors have been extensively examined. However, the fidelity of control on those spins is not high enough for practical use due to their fast orbital relaxation.

In this article, we demonstrate optically addressable high-fidelity manipulations of an electron spin by combining global microwave manipulation and local optical Stark shift using a nitrogen-vacancy (NV) center in diamond. We also demonstrate that the optically addressable manipulation of the electron spin is utilized to selectively manipulate the nuclear spin of the nitrogen atom constituting the NV center and even to control the interaction between the electron and nuclear spins. Finally, we demonstrate quantum entanglement generation between the electron and nuclear spins to prepare for the quantum state transfer^{28,29} of a photon state into the nuclear spin state of the nitrogen quantum memory. The developed scheme satisfies all of the DiVincenzo criteria³⁰ including not only scalability, initialization, measurement, universal gate, and long coherence but also interqubit connectivity with a photon.

II. System and scheme

The negatively charged NV center has a hybridized level structure of an electron orbital with a spin-1 electron spin. The orbital ground state has a degenerate V-shaped three-level spin structure. At zero magnetic field, $|\pm 1\rangle_s$ states with magnetic quantum numbers $m_s = \pm 1$ are degenerate, and $|0\rangle_s$ state with $m_s = 0$ energetically splits from $|\pm 1\rangle_s$ of about 2.88 GHz. We here define $|\pm 1\rangle_s$ as the computational bases for a qubit. There is no direct magnetic transition between the two qubit bases. Instead, there is a transition between a bright state $|B\rangle_s$ and an ancilla state $|0\rangle_s$ depending on the polarization of the microwave field, while a dark state $|D\rangle_s$ remains unchanged. A cyclic evolution in a bright space $\{|B\rangle_s, |0\rangle_s\}$ induces a geometric phase γ to $|B\rangle_s$ depending on the trajectory of the space. That allows the qubit to rotate γ around the $|B\rangle_s - |D\rangle_s$ axis to realize a universal single qubit gate^{31,32}.

The key idea of this work is to induce an optical Stark shift in the ancilla state $|0\rangle_s$ to correlate the microwave frequency

resonant to the bright space with optical intensity (Fig. 1a). One of the orbital excited states $|E_y\rangle$ is allowed to make an optically coherent transition from $|0\rangle_s$ at low temperature. Detuning the laser frequency from the energy gap between $|E_y\rangle$ and $|0\rangle_s$ suppresses their optical transition to induce repulsive energy shifts owing to the optical Stark effect (Fig. 1b). The shift results in the modulation of the resonance frequency between $|B\rangle_s$ and $|0\rangle_s$ in the bright space, which is observed by the optically detected magnetic resonance (ODMR) (Fig. 1c) spectrum or Ramsey interference (see methods) of the electron spin. The optical Stark shift Δ_S depends on the laser detuning Δ_L and the optical power or Rabi frequency Ω_L , and is approximated by $\Delta_S \approx \Omega_L^2/4\Delta_L$, provided that $\Omega_L \ll \Delta_L$. Note that the optical Stark shift does not change the degeneracy of the qubit space and thus we cannot directly manipulate the qubit. On the other hand, a microwave tuned to the frequency shift in the bright space enables selective manipulation of the qubit. Although $\Omega_{MW} \ll \Delta_S$ is required for high frequency selectivity, in practice, there is an upper limit for Δ_S given by the condition $\Omega_L \ll \Delta_L$ to suppress the optical absorption. Moreover, Ω_{MW} cannot be reduced because of the inhomogeneous broadening of $|\pm 1\rangle_s$ due to hyperfine interactions with environmental nuclear spins.

Therefore, we develop an amplitude-alternating microwave pulse that works either as an identity operation or a rotation operation depending on whether the microwave is on or off the resonance frequency even with the small frequency difference (see methods). The amplitude-alternating pulse reverses the amplitude (or shifts the relative phase by π) at the middle point of a square envelope pulse. In the absence of the optical Stark shift without the addressing laser, the microwave is on resonance, and thus the bright state $|B\rangle_s$ rotates along a great circle in the Bloch sphere representing the bright space in the first half of the pulse and then reverses the rotation to cancel the first rotation and returns to $|B\rangle_s$ in the second half of the pulse (Fig. 1e). On the other hand, in the presence of the optical Stark shift with the addressing laser, the microwave is off resonance and thus $|B\rangle_s$ rotates along two adjacent small circles in a figure of eight and returns to $|B\rangle_s$ (Fig. 1f). As a result, $|B\rangle_s$ obtains a geometric phase proportional to the solid angle enclosed by the trajectory of the Bloch vector as

$$\gamma = 2\pi \left(1 - \frac{\Delta_S}{\sqrt{\Omega_{MW}^2 + \Delta_S^2}} \right), \quad (1)$$

where the pulse length is

$$t_{\text{MW}} = \frac{4\pi}{\sqrt{\Omega_{\text{MW}}^2 + \Delta_S^2}} \quad (2)$$

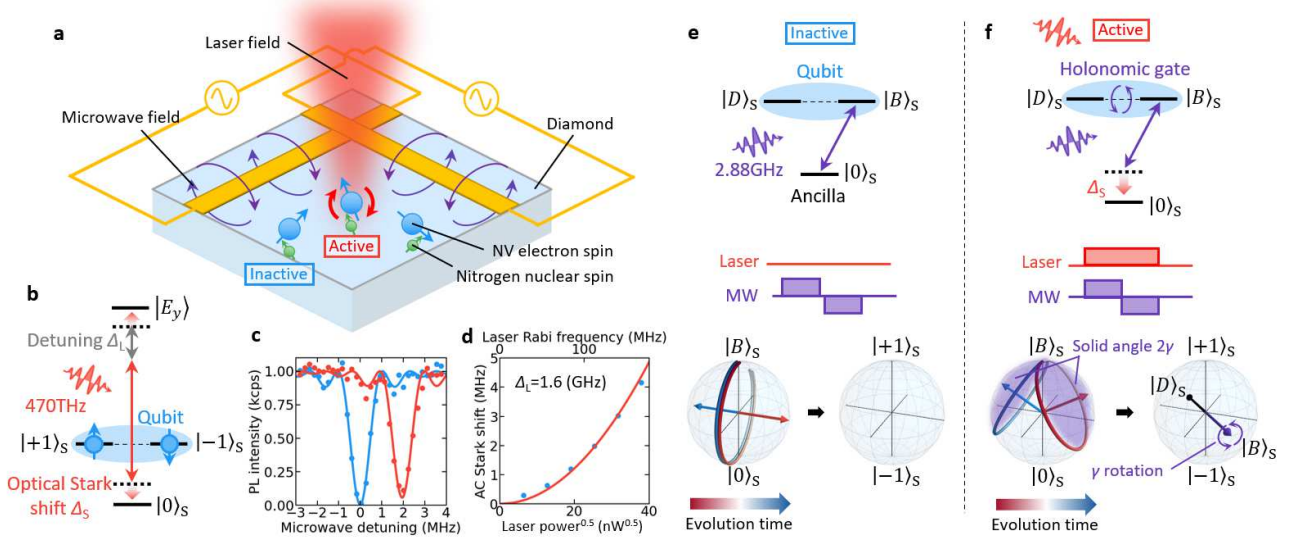


FIG. 1 | Principle of optically addressable universal holonomic gates. **a**, Schematic of the optically addressable gate with the device geometry. A laser activates the microwave-driven gate on the electron spin. **b**, Electronic level structure with spin sub-levels of the NV center. The spin sub-levels $|m_s = \pm 1\rangle$ constitute the qubit bases. The ancilla spin sub-level $|m_s = 0\rangle_s$ is frequency shifted by the optical Stark effect with the detuned laser. **c**, ODMR spectrum showing the frequency shift. **d**, Optical Stark shift as a function of the laser power. **e**, Spin dynamics without the addressing laser. An amplitude-alternating microwave pulse drives the bright state to rotate in a great circle within the bright $|B\rangle_s$ and ancilla $|0\rangle_s$ states and return to the original state $|B\rangle_s$ in the bright space. **f**, Spin dynamics with the addressing laser. The same microwave pulse induces a figure-8 motion and returns to the original state in the bright space, resulting in state rotation around $|B\rangle_s$ in the qubit space by the geometric phase γ defined by the solid angle of the trajectory in the bright space.

III. Optical addressability

We first demonstrate that the addressing laser properly switches between the two gate operations on the electron spin. The details of the experimental setup are described in the methods section. The optical Stark shift is targeted to $\Delta_S = 4$ MHz given by $\Omega_L = 160$ MHz and $\Delta_L = 1.6$ GHz, which are optimized so that $T_2^{\text{Stark}} \Delta_S$ indicating the quality of the frequency shift becomes as large as possible. The amplitude-alternating microwave pulse is set to show a Rabi frequency of $\Omega_{\text{MW}} = 4\sqrt{3}$ MHz with a pulse width of $t_{\text{MW}} = 250$ ns so that the qubit rotates by π in the qubit space. If the irradiated laser power is adequate, the initial state $|+\rangle_s$ should rotate into $|-\rangle_s$. On the other hand, if the laser power is sufficiently small, the state should return to the original $|+\rangle_s$ (Fig. 2a, b). Figures 2c and 2d show the populations of the final state as functions of the laser and microwave powers. The measurements agree well with the simulations. Note that even if the microwave power

is not necessarily optimal, the gate operation is inactive as long as the laser power is small enough. The scheme is significant in the practical situation that microwave antennas cannot generate spatially uniform field.

We next demonstrate gate contrast depending on the NV position. We measure the spatial distribution of the optical Stark shift by displacing the focal point of the addressing laser off the NV center, resulting in a steep reduction of the shift (Fig. 2e). The distribution is well fitted by a Gaussian function with a standard deviation of 247 nm, which is consistent with the spatial distribution of the laser power. With this distribution, the spatial distributions of $|\pm 1\rangle_s$ probabilities after the gate operation (Fig. 2f) are inferred from the probability dependence on the laser Rabi frequency shown in Fig. 2c, d.

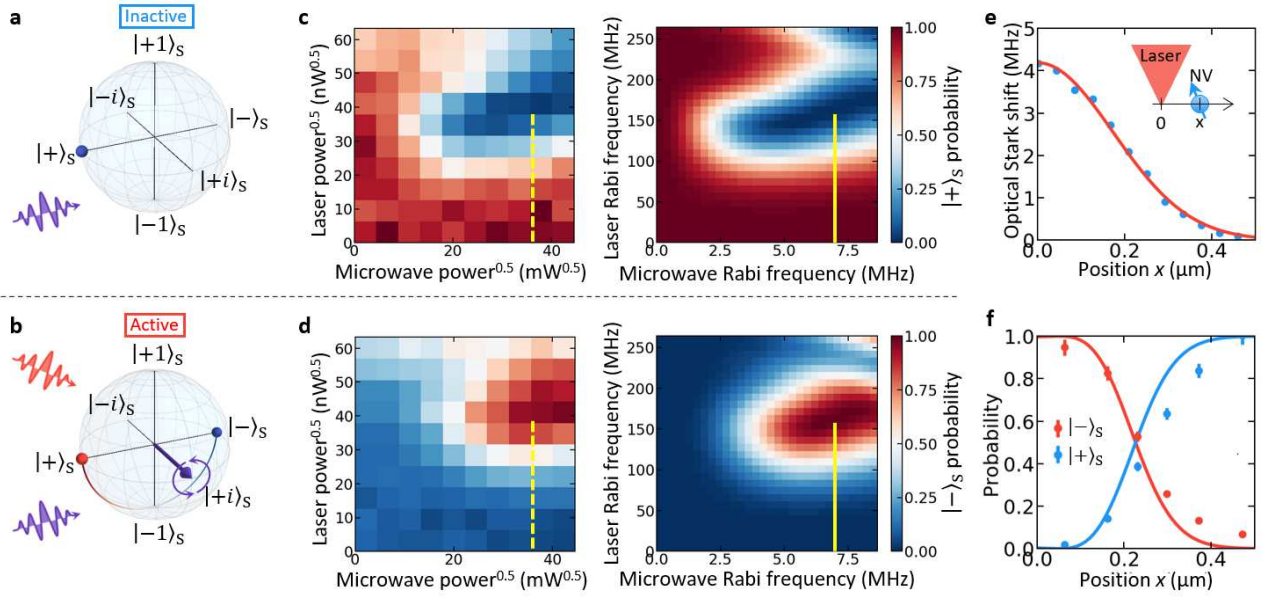


FIG. 2 | Experimental demonstration of the gate contrast depending on the laser power or the NV position **a, b**, Bloch sphere representation of the transition of the $|+\rangle_s$ state by optically addressable Pauli-Y gate. **a**, Without the addressing laser, the $|+\rangle_s$ state remains in the original state. **b**, With the addressing laser, the $|+\rangle_s$ state transitions to the $|-\rangle_s$ state. **c, d**, Laser and microwave power dependence of the optically addressable Pauli-Y gate and the corresponding simulations. **c** shows the population of the $|+\rangle_s$ state after the gate operation, and **d** shows the population of the $|-\rangle_s$ state after the gate operation. **e**, The frequency shift induced by the optical Stark effect as a function of the NV position. Dots show measured data, and the line shows a fit to the Gaussian distribution. **f**, Probabilities of the $|\pm 1\rangle_s$ states after the gate operation inferred from **e** as a function of the NV position. Dots are estimated from the measurements along the yellow dashed line in **c** and **d**. Lines are estimated from the simulation along the yellow solid line in **c** and **d**. Error bars are standard deviations.

IV. Optically addressable universal single qubit operation

We then demonstrate the universality of single quantum gates by showing the Pauli-X, Y, and Z gate operations conditioned by laser irradiation. The Pauli-X, Y, Z gates require the geometric phase shift $\gamma = \pi$, leading to the condition

for the laser power corresponding to $\Omega_{\text{MW}} = \sqrt{3}\Delta_s$, and the pulse width $t_{\text{MW}} = 1/\Delta_s$. We set $\Delta_s = 2$ MHz, $\Omega_{\text{MW}} = 2\sqrt{3}$ MHz and $t_{\text{MW}} = 500$ ns due to the upper limitation of Ω_{MW} in our current microwave setup. The gate fidelities are estimated by quantum process tomography with (active) and without (inactive) the addressing laser. Figures 3a,b,c guarantee fidelities over 90% in any situations showing the Pauli-X, Y, and Z gate and identity operations. Even though the gate time is not sufficiently short compared to the spin coherence time $T_2^* \sim 3\mu\text{s}$, the spin coherence after the gate operation is well maintained even in the inactive case. This is because the driving microwave suppresses the non-commutable phase relaxation induced by a ^{13}C nuclear spin bath, except for the Pauli-Z gate, where the drive Hamiltonian is commutable with the phase relaxation. We also show optically addressable preparation (Fig. 3d) and readout (Fig. 3e) of the X, Y and Z basis states in the qubit space by the amplitude-alternating microwave pulse as well as the gate operation. Although the success probabilities are not extremely high in the active case, the error probabilities are extremely low in inactive case, which enables high-fidelity initialization conditioned by the addressing laser irradiation (Fig. 3f) (see methods). We also show that the coherence can be maintained by a spin echo using an optically addressable gate (Fig. 3g).

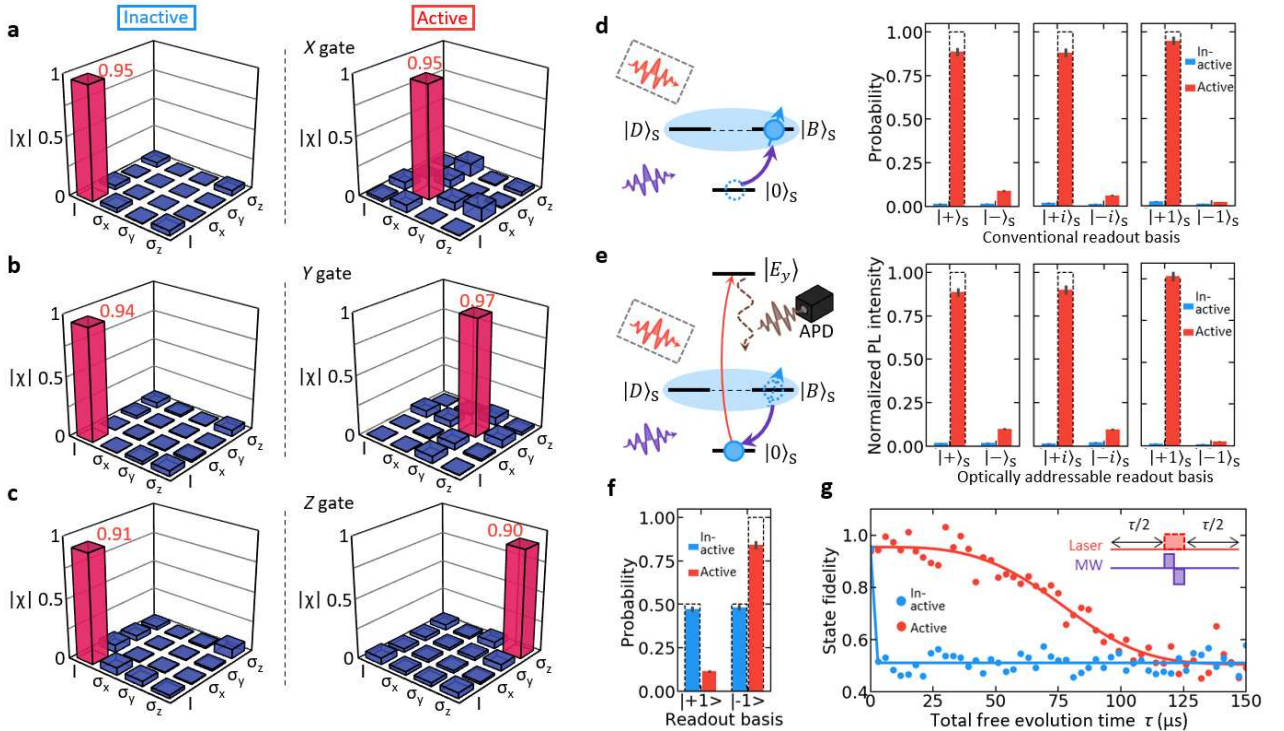


FIG. 3 | Experimental demonstration of optically addressable universal single qubit operations. **a, b, c**, χ -matrices reconstructed by quantum process tomography without (left)/with (right) laser irradiation showing identity and Pauli-X, Y, and Z gate operations. Red (blue) bars are elements with unity (zero) values in the ideal gate. **d, e**, Schematics and experimental results showing optically addressable quantum state preparation (d) and readout (e). **f**, Experimental results showing optically addressable quantum state

initialization. The initialization is performed on the maximally mixed state (see methods). **g**, Experimental results showing spin echo with optically addressable Pauli-Y gate. The pulse sequence is shown in the inset. Lines show the fitted decay curve with $\exp[-(\tau/T_2)^p]$. Error bars show standard deviations.

V. Optically addressable quantum entanglement generation

We finally demonstrate the optically addressable entanglement generation between the electron and nitrogen nuclear spins, as a component of a quantum state transfer^{28,29} from an entangled photon^{33–35} into a nuclear spin quantum memory. We utilize optically addressed electron spin to activate or deactivate the nuclear spin gate operations. Conditioned by the electron spin to be in $|0\rangle_S$, the nuclear spin is universally manipulated with polarized radiowave within the three-level structure as that of the electron spin (see methods). The pulse sequence is shown in Fig. 4a, d. The initial state prepared in $|+1, 0\rangle_{S,N}$ is optically selectively transferred to $|0, 0\rangle_{S,N}$ by the developed manipulation shown in Fig. 3e. After the nuclear spin rotation to $|+\rangle_N$ conditioned by the $|0\rangle_S$ state, the DCNOT gate²⁸ generates an entangled state $|\psi^+\rangle = (|+1, -1\rangle_{S,N} + |-1, +1\rangle_{S,N})/\sqrt{2}$ (Fig. 4b). The DCNOT gate uses an optimized waveform generated by the GRAPE algorithm to increase the gate fidelity³¹. In case that the addressing laser is not irradiated, the nuclear spin state remains unchanged since the electron spin is in the qubit space (Fig. 4e). We estimate the nuclear spin state by quantum state tomography with (active) and without (inactive) the addressing laser under the same microwave and radio wave conditions. Figures 4c and 4f show that the fidelities of $|+1, 0\rangle_{S,N}$ and $|\psi^+\rangle$ are respectively 83.4% and 91.1% in the inactive and active cases. The degradation of the fidelity is mainly due to unexpected dynamics of the electron spin even when the nuclear spin is in $|0\rangle_N$ during the DCNOT gate. Although the specific state $|+1, 0\rangle_{S,N}$ is prepared in the demonstration, we can apply the optically addressable entanglement generation scheme to any arbitrary states including entangled states with other qubits.

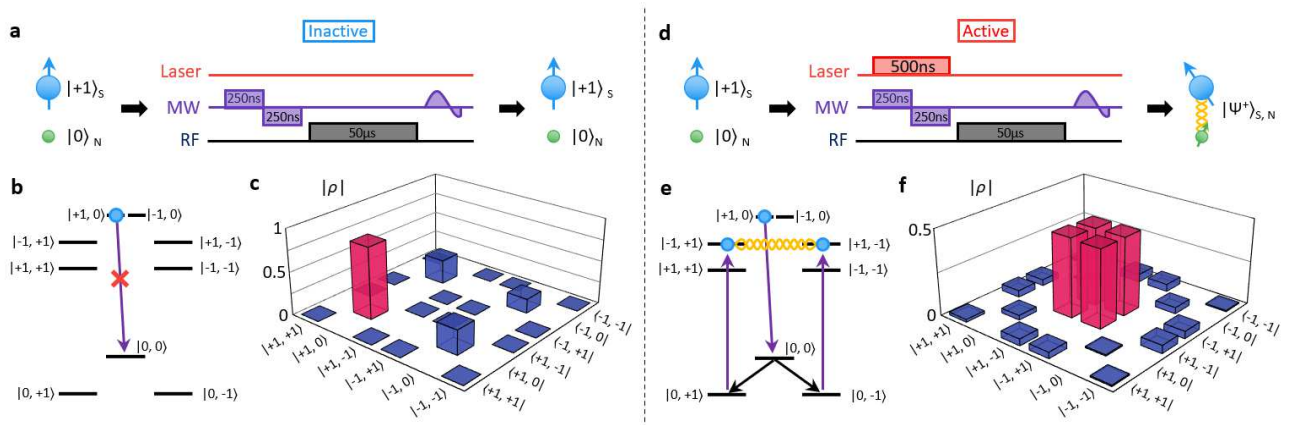


FIG. 4| Optically addressable entanglement generation. **a, d**, Pulse sequence for optically addressable entanglement generation. The initial state is prepared in $|+1,0\rangle_{S,N}$. Without (with) the laser, the electron spin remains (transitions) in $|+1\rangle_S$ to inactivate (activate) the nuclear spin manipulation. The subsequent DCNOT produces an entangled state only in the active case. **b, e**, Energy level structures and the state transitions of electron-nitrogen nuclear spins in an NV center. **c, f**, Absolute value of the density matrix obtained by quantum state tomography. In the ideal states, the values of the red bars are 1 (**c**) and 0.5 (**f**).

VI. Discussion and conclusion

The amplitude-alternating microwave pulse developed in this study can be applied not only to the optical Stark shift but also to the gradient magnetic field scheme to individually manipulate qubits with different resonance frequencies. It also serves simply as a quantum gate that is extremely robust against Rabi frequency errors (see Methods). The reason for the improved fidelity of our scheme over all-optical schemes is the use of an excess degree of freedom that is easier to control. Other techniques such as composite pulses³⁶ and numerically optimized waveforms³⁷ are also applicable to further improve the fidelity of two-qubit gates, which is much harder than for single-qubit gates.

Since the laser irradiation itself does not change the state of the qubit, unlike in the conventional all-optical approach, the spatial resolution can be further increased by using the strong gradient spot or donut-shaped beam. By increasing the resolution to several tens of nanometers, it will be possible to selectively control multiple NV centers in the strongly coupled regime³⁸. The demonstration combined with optically coherent NV center formation methods³⁹⁻⁴¹ and real-time optical deflection techniques⁴²⁻⁴⁴ will enable selective access of more than 10,000 qubits in a $10\times 10\times 10\ \mu\text{m}$ image volume, paving the way for large-scale quantum storage.

VII. Methods

Experimental setup. The experiments in this work use a single naturally occurring NV center in a high-purity type-IIa electric grade diamond with crystal orientation $\langle 100 \rangle$ grown by Element Six. The diamond is cooled to 5 K for coherent control of the electron orbital. A home-built confocal microscope system is used to address the single NV center in the same manner as in Sekiguchi et al.³⁵. A green laser probabilistically resets the charge state. A spin pumping by the resonant excitation to $|E_{1,2}\rangle$ initializes the electron spin state into $|0\rangle_S$. To readout the electron spin qubit state, the phonon sideband emissions induced by the resonant excitations to $|E_y\rangle$ are detected by an avalanche photodiode after the transformation between the readout basis and $|0\rangle_S$ using a microwave π -pulse. The power of the addressing laser for the optical Stark

shift is monitored before the objective lens to be stabilized to within 0.1% by PID control. Two orthogonal wires are attached over the diamond surface to utilize the polarization degrees of freedom of the microwave and radiowave. The environmental magnetic field is canceled by a 3D coil to achieve a zero magnetic field. In order to reduce the inhomogeneous broadening of the resonance frequency of the electron spin due to the hyperfine interaction with the nuclear spins, the nitrogen nuclear spin is initialized to $|m_I = 0\rangle_N$ in all experiments in this work.

Amplitude-alternating microwave pulse. The rotating frame Hamiltonian of the V-shaped three-level system under the microwave irradiation with detuning Δ and Rabi frequency Ω_{MW} is given by

$$\begin{aligned} H_V^\pm &= \frac{\pm\Omega_{MW}}{2}(|0\rangle_S\langle B| + |B\rangle_S\langle 0|) - \Delta|0\rangle_S\langle 0| \\ &= \frac{\Omega_{\text{eff}}}{2}\mathbf{n}^\pm \cdot \boldsymbol{\sigma}^{\{0,B\}} - \frac{\Delta}{2}\sigma_0^{\{0,B\}}, \end{aligned} \quad (3)$$

where $\Omega_{\text{eff}} = \sqrt{\Omega_{MW}^2 + \Delta^2}$ is the effective Rabi frequency, $\mathbf{n}^\pm = \left(\pm\frac{\Omega}{\Omega_{\text{eff}}}, 0, -\frac{\Delta}{\Omega_{\text{eff}}}\right)$ is a unit vector indicating the rotation axis, $\boldsymbol{\sigma}^{\{0,B\}} = \left(\sigma_x^{\{0,B\}}, \sigma_y^{\{0,B\}}, \sigma_z^{\{0,B\}}\right)$, $\sigma_{0,x,y,z}^{\{0,B\}}$ are the Pauli operators and identity operator based on $|0\rangle_S$, $|B\rangle_S$, and $|B\rangle_S = \cos\theta_{MW}|+1\rangle_S + e^{-i\phi_{MW}}\sin\theta_{MW}|-1\rangle_S$ is a bright state depending on the microwave polarization $|\psi\rangle_{MW} = \cos\theta_{MW}|+1\rangle_{MW} + e^{-i\phi_{MW}}\sin\theta_{MW}|-1\rangle_{MW}$, where θ_{MW} , ϕ_{MW} are a polar and an azimuth angle in Poincaré sphere spanned by a right $|+1\rangle_{MW}$ and a left $|-1\rangle_{MW}$ circular polarization. The \pm indicates a positive and negative microwave amplitude or a microwave phase of 0 and π . The time evolution operator as a function of time is

$$U_V^\pm(t) = \exp\left(-i\frac{\Omega_{\text{eff}}t}{2}\mathbf{n}^\pm \cdot \boldsymbol{\sigma}^{\{0,B\}}\right) \exp\left(i\frac{\Delta t}{2}\right) + |D\rangle_S\langle D|. \quad (4)$$

The total time evolution of the amplitude-alternating pulse, which reverses the amplitude in the middle of the pulse with a pulse time width $t_{MW} = \frac{4\pi}{\Omega_{\text{eff}}}$ is

$$U_V^-\left(\frac{t_{MW}}{2}\right)U_V^+\left(\frac{t_{MW}}{2}\right) = \exp\left\{\frac{2i\pi\Delta}{\Omega_{\text{eff}}}\right\}\sigma_0^{\{0,B\}} + |D\rangle_S\langle D|. \quad (5)$$

This means that the qubit spanned by $|\pm 1\rangle_S$ is rotated by an angle $\frac{2i\pi\Delta s}{\Omega_{\text{eff}}}$ around the $|B\rangle_S$ - $|D\rangle_S$ axis. Therefore, if $\Delta \neq 0$, arbitrary rotation is enabled by choosing the appropriate microwave polarization and pulse width. On the other hand, if $\Delta = 0$, the identity operator is strictly implemented. Figure 5 shows the numerical calculations of the fidelity of frequency

dependent unitary evolution with the amplitude-alternating pulse and the simple square envelope pulse. The calculations do not take into account the effects of phase relaxation induced by the ^{13}N and ^{13}C nuclear spin bath and the orbital relaxation. The amplitude-alternating pulse is extremely robust against Rabi frequency error, especially where the Rabi frequency is too large.

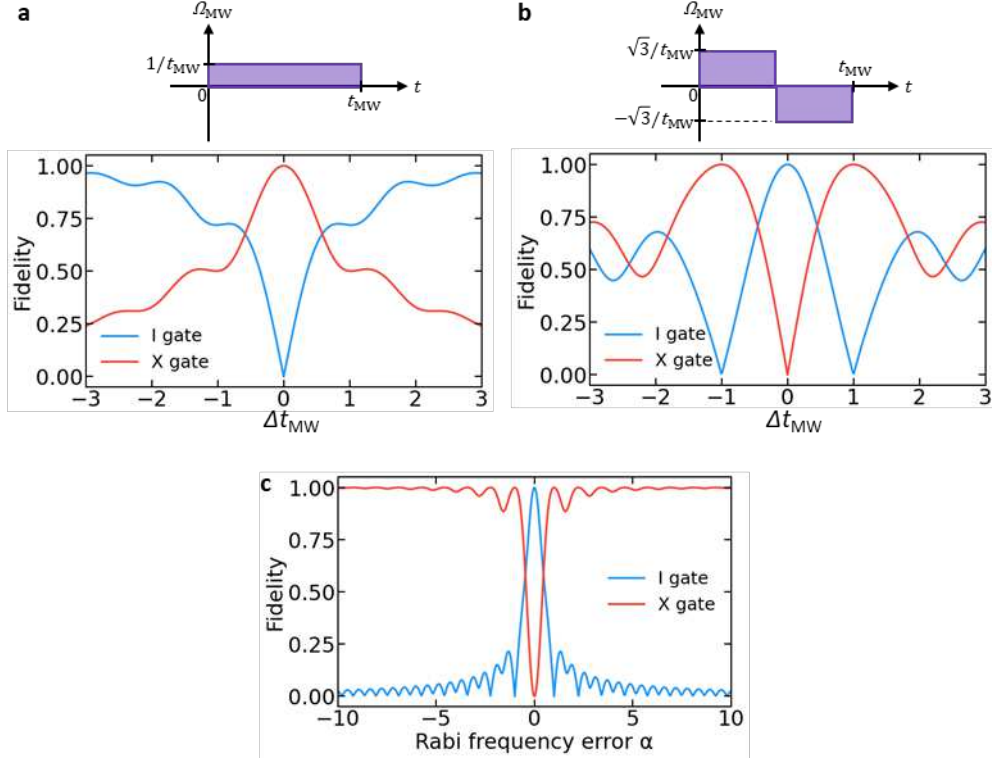


FIG. 5| Simulations of the process fidelity. **a, b**, Fidelity of the X and identity (I) gates implemented by **(a)** a square envelope pulse and **(b)** an amplitude-alternating pulse as a function of Δt_{MW} . The top graphs show the time dependence of the microwave Rabi frequency Ω_{MW} . **c**, Process fidelity as a function of Rabi frequency error α , which denotes the magnification from ideal Rabi frequency Ω_0 as $\Omega_{\text{MW}} = \alpha\Omega_0$. The gate fidelity is defined as $|\text{Tr}(U_s^\dagger U_i)|/2$, where U_i and U_s denote an ideal gate and a simulated gate.

Optimization of the optical Stark shift. Since the optical Stark shift utilizes the orbital perturbation, the accompanying spin state is affected by the orbital relaxation to cause a phase relaxation. Hence, it is important to select the experimental parameters appropriately to achieve the best performance of the gates. In order to suppress the phase relaxation due to the orbital relaxation, the ratio of the detuning Δ_L to the optical Rabi frequency Ω_L must be sufficiently large. Moreover, there are other requirements: Δ_L should be smaller than the energy gap of the orbital fine structure, and Ω_L should be large enough to induce a larger frequency shift than inverse of intrinsic spin relaxation time. However, since it is difficult to solve the optimal parameters analytically, we experimentally evaluate the quality of the optical Stark shift, which is defined as $\mathcal{A}_S T_2^{\text{Stark}}$. The optical Stark shift \mathcal{A}_S and coherence time T_2^{Stark} were obtained by fitting the Ramsey interference

prepared in the initial state $(|+1\rangle_s + |0\rangle_s)/\sqrt{2}$ with an exponentially decaying sinusoidal wave. Based on the obtained two-dimensional color map, reasonable Δ_L and Ω_L are selected according to the required Δ_S in the main text. In practice, in order to precisely adjust Δ_S to the target value, the laser power or Ω_L is swept while Δ_L is fixed.

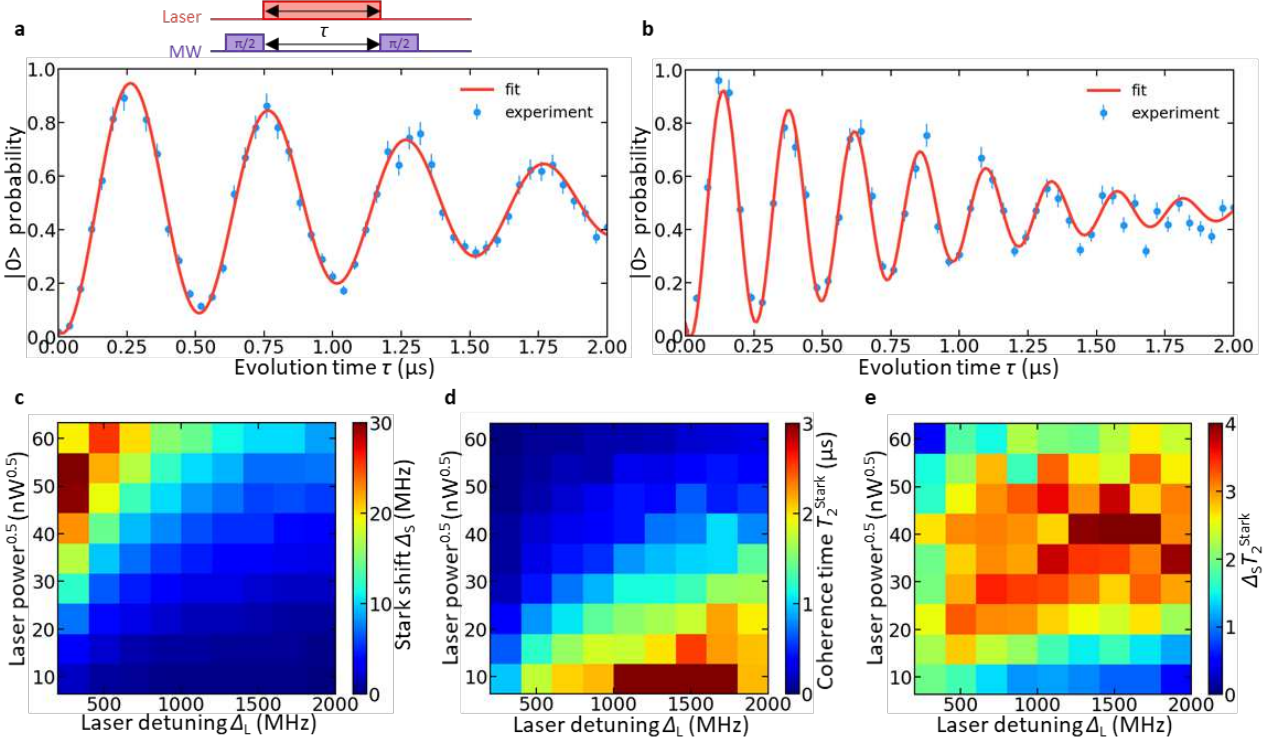


FIG. 6 | Ramsey interference induced by an optical Stark shift. **a**, Ramsey interference at the laser power of 1440 nW and the detuning of 1.6 GHz. After initializing the spin to $|0\rangle_s$, the addressing laser is irradiated during the free evolution time between $\pi/2$ pulses of the Ramsey interference (Top). **b**, Ramsey interference at the laser power of 640 nW and the detuning of 1.6 GHz. **c**, Stark shift Δ_S as functions of the laser power and detuning. **d**, Coherence time in the bright space T_2^{Stark} as functions of the laser power and detuning. **e**, Their product $\Delta_S T_2^{\text{Stark}}$ as functions of the laser power and detuning.

Optically addressable electron spin initialization. The electron spin of the NV center at low temperature is typically initialized by spin pumping with spin-selective optical excitation. In this method, the resolution is limited to the spot size of the light, since the initialization is applied over the entire area irradiated by light. We here present an initialization method using a pulse sequence combining light and microwave, which in principle can achieve a resolution below the diffraction limit of light. Figure 7 shows the pulse sequence used in Fig. 3f. $|+1\rangle_s$ is selectively transitioned to $|0\rangle_s$ by optically addressable manipulation. Then, the resonant excitation to $|E_y\rangle$ relaxes the spin state $|0\rangle_s$ to $|\pm 1\rangle_s$ in a half-and-half ratio. This process results in pumping only a half of the population of $|+1\rangle_s$ into $|-1\rangle_s$. In the experiment, this cycle is repeated 10 times. For comparison, the initial state is prepared in a completely mixed state, and the spin state is measured

after the initialization sequence is run. The reason why the bias of the spin state in the inactive case is kept small is that the error of optically addressable transition in the inactive case is very small, as shown in Fig. 3e.

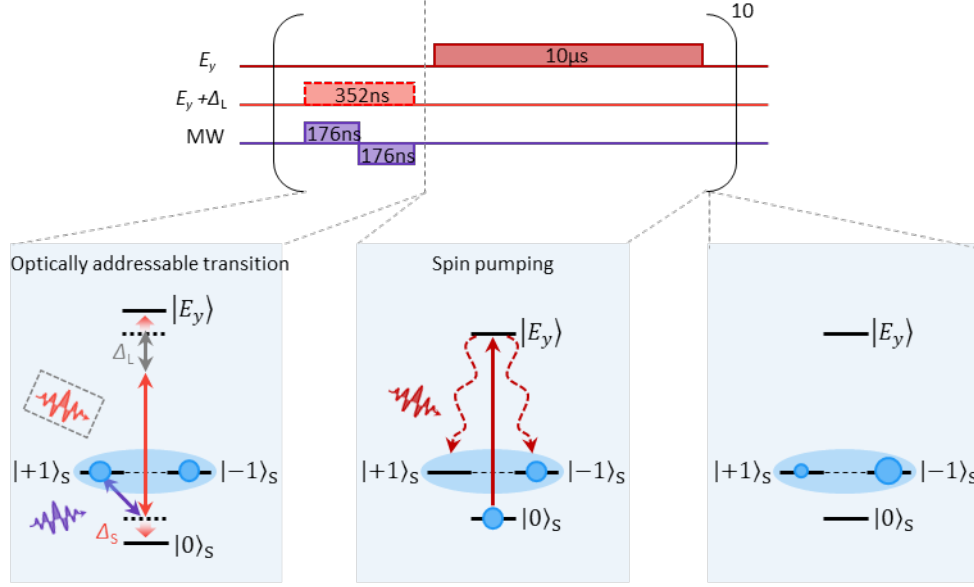


FIG. 7 | Experimental sequence of an optically addressable initialization. First, the optically addressable manipulation transfers $|+1\rangle_s$ into $|0\rangle_s$ by the addressing laser for the optical stark shift of $\Delta_s = 2$ MHz (given by $\Omega_L = 80\sqrt{2}$ MHz and $\Delta_L = 1.6$ GHz) and the amplitude-alternating microwave pulse with Rabi frequency of $\Omega_{MW} = 2$ MHz. Next, a spin pumping by a resonant excitation to $|E_y\rangle$ equally distributes the $|0\rangle_s$ population into $|\pm 1\rangle_s$. This process is repeated 10 times.

Optically addressable nuclear spin manipulations. We control whether or not to activate the nitrogen (^{14}N) nuclear spin operation via optically addressable electron spin since the light does not interact with the nuclear spin. When the electron spin is in the ancilla state $|0\rangle_s$, the nuclear spin constitutes a degenerate Λ -shaped three-level structure induced by a nuclear quadrupole splitting of 4.95 MHz. In that subspace, an arbitrary single qubit gate is feasible with the resonant radiowave in a way similar to the electron spin. On the other hand, when the electron spin is in the qubit space $|\pm 1\rangle_s$, the nuclear spin is split by the hyperfine interaction and thus it does not respond to a radiowave with the same frequency. Figure 8a shows the experimental sequence for demonstration of the optically addressable nuclear spin operations. We first initialize the nuclear spin in the ancilla state $|m_I = 0\rangle_N$ to show that the subsequent state preparation into qubit state $|m_I = \pm 1\rangle_N$ is activated by the light (Fig. 8b). The fidelities of the prepared states are comparable to those in the previous work³¹. Next, we apply holonomic quantum gates on the prepared states to perform quantum process tomography. The averaged fidelity of the gates is 98%, which is also comparable to the previous work. In the quantum process tomography,

only the activated states are taken into account. In our demonstrations, although the inactive nuclear spin state is $|0\rangle_N$ and the electron spin is conditioned to be in $|+1\rangle_s$, in principle, unconditional gate operations for the electron-nuclear spin qubit system are feasible. However, due to the long manipulation time of the nuclear spin, it is necessary to combine the holonomic gate with a dynamical decoupling to preserve the coherence of the electron spin.

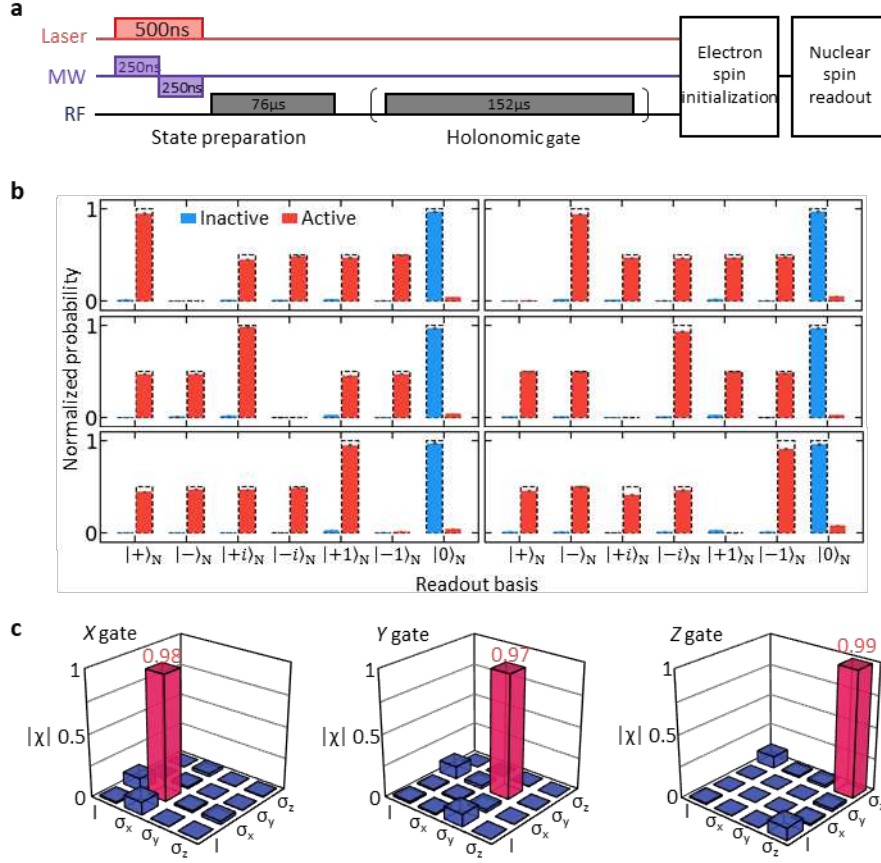


FIG. 8| Optically addressable nuclear spin manipulations. **a**, Experimental sequence of quantum state tomography and quantum process tomography shown in **b**, **c**. First, optically addressable electron spin manipulation is performed to an initial state of $|0, 0\rangle_{s,N}$. When the electron spin is in $|0\rangle_s$ ($|\pm 1\rangle_s$) the nuclear spin manipulation is active (inactive). After the manipulations, the electron spin is initialized to $|0\rangle_s$ to readout the nuclear spin state by the repetitive readout of electron spin with CNOT-like gates. **b**, State probabilities of the six prepared states $\{|+\rangle_N = (|+1\rangle_N + |+1\rangle_N)/\sqrt{2}, |-\rangle_N = (|+1\rangle_N - |+1\rangle_N)/\sqrt{2}, |+i\rangle_N = (|+1\rangle_N + i|+1\rangle_N)/\sqrt{2}, |-i\rangle_N = (|+1\rangle_N - i|+1\rangle_N)/\sqrt{2}, |+1\rangle_N, |-1\rangle_N\}$. Without the addressing laser, the nuclear spin state stays in $|0\rangle_s$. **c**, Absolute values of χ matrix elements reconstructed by the quantum process tomography for the optically addressable Pauli-X, Y, Z gate. Red (blue) bars are elements with unity (zero) values in the ideal state.

ACKNOWLEDGEMENTS

We thank Hiromitsu Kato, Toshiharu Makino, Tokuyuki Teraji, Yuichiro Matsuzaki, Kae Nemoto, Norikazu Mizuochi, Fedor Jelezko, and Joerg Wrachtrup for their discussions and experimental help. This work was supported by Japan Society for the Promotion of Science (JSPS) Grants-in-Aid for Scientific Research (20H05661, 20K2044120); by Japan Science and Technology Agency (JST) CREST (JPMJCR1773); and by JST Moonshot R&D (JPMJMS2062). We also acknowledge the assistance of the Ministry of Internal Affairs and Communications (MIC) under the initiative Research and Development for Construction of a Global Quantum Cryptography Network (JPMI00316).

References

1. Balasubramanian, G. *et al.* Ultralong spin coherence time in isotopically engineered diamond. *Nature Materials* **8**, 383–387 (2009).
2. Bar-Gill, N., Pham, L. M., Jarmola, A., Budker, D. & Walsworth, R. L. Solid-state electronic spin coherence time approaching one second. *Nature Communications* **4**, 1743 (2013).
3. Aboeih, M. H. *et al.* One-second coherence for a single electron spin coupled to a multi-qubit nuclear-spin environment. *Nature Communications* **9**, 2552 (2018).
4. Herbschleb, E. D. *et al.* Ultra-long coherence times amongst room-temperature solid-state spins. *Nature Communications* **10**, 3766 (2019).
5. Bradley, C. E. *et al.* A Ten-Qubit Solid-State Spin Register with Quantum Memory up to One Minute. *Physical Review X* **9**, 031045 (2019).
6. Nguyen, C. T. *et al.* An integrated nanophotonic quantum register based on silicon-vacancy spins in diamond. *Physical Review B* **100**, 165428 (2019).
7. Pioro-Ladrière, M., Tokura, Y., Obata, T., Kubo, T. & Tarucha, S. Micromagnets for coherent control of spin-charge qubit in lateral quantum dots. *Applied Physics Letters* **90**, 024105 (2007).
8. Foletti, S., Bluhm, H., Mahalu, D., Umansky, V. & Yacoby, A. Universal quantum control of two-electron spin quantum bits using dynamic nuclear polarization. *Nature Physics* **5**, 903–908 (2009).
9. Arai, K. *et al.* Fourier magnetic imaging with nanoscale resolution and compressed sensing speed-up using electronic spins in diamond. *Nature Nanotechnology* **10**, 859–864 (2015).
10. Yamamoto, T. *et al.* Strongly coupled diamond spin qubits by molecular nitrogen implantation. *Physical Review B* **88**, 201201 (2013).
11. Haruyama, M. *et al.* Triple nitrogen-vacancy centre fabrication by C₅N₄Hn ion implantation. *Nature Communications* **10**, 2664 (2019).
12. Robledo, L. *et al.* High-fidelity projective read-out of a solid-state spin quantum register. *Nature* **477**, 574–578 (2011).
13. Irber, D. M. *et al.* Robust all-optical single-shot readout of nitrogen-vacancy centers in diamond. *Nature Communications* **12**, 532 (2021).

14. Golter, D. A. & Wang, H. Optically Driven Rabi Oscillations and Adiabatic Passage of Single Electron Spins in Diamond. *Physical Review Letters* **112**, 116403 (2014).
15. Bassett, L. C. *et al.* Ultrafast optical control of orbital and spin dynamics in a solid-state defect. *Science* **345**, 1333–1337 (2014).
16. Chu, Y., Markham, M., Twitchen, D. J. & Lukin, M. D. All-optical control of a single electron spin in diamond. *Physical Review A* **91**, 021801 (2015).
17. Goldman, M. L., Patti, T. L., Levonian, D., Yelin, S. F. & Lukin, M. D. Optical Control of a Single Nuclear Spin in the Solid State. *Physical Review Letters* **124**, 153203 (2020).
18. Lekavicius, I., Golter, D. A., Oo, T. & Wang, H. Transfer of Phase Information between Microwave and Optical Fields via an Electron Spin. *Physical Review Letters* **119**, 063601 (2017).
19. Berezovsky, J., Mikkelsen, M. H., Stoltz, N. G., Coldren, L. A. & Awschalom, D. D. Picosecond Coherent Optical Manipulation of a Single Electron Spin in a Quantum Dot. *Science* **320**, 349–352 (2008).
20. Buckley, B. B., Fuchs, G. D., Bassett, L. C. & Awschalom, D. D. Spin-light coherence for single-spin measurement and control in diamond. *Science* **330**, 1212–1215 (2010).
21. Press, D., Ladd, T. D., Zhang, B. & Yamamoto, Y. Complete quantum control of a single quantum dot spin using ultrafast optical pulses. *Nature* **456**, 218–221 (2008).
22. Greilich, A. *et al.* Ultrafast optical rotations of electron spins in quantum dots. *Nature Physics* **5**, 262–266 (2009).
23. Kodriano, Y. *et al.* Complete control of a matter qubit using a single picosecond laser pulse. *Physical Review B* **85**, 241304 (2012).
24. Yale, C. G. *et al.* Optical manipulation of the Berry phase in a solid-state spin qubit. *Nature Photonics* **10**, 184–189 (2016).
25. Sekiguchi, Y., Niikura, N., Kuroiwa, R., Kano, H. & Kosaka, H. Optical holonomic single quantum gates with a geometric spin under a zero field. *Nature Photonics* **11**, 309–314 (2017).
26. Zhou, B. B. *et al.* Holonomic Quantum Control by Coherent Optical Excitation in Diamond. *Physical Review Letters* **119**, 140503 (2017).
27. Ishida, N. *et al.* Universal holonomic single quantum gates over a geometric spin with phase-modulated polarized light. *Optics Letters* **43**, 2380 (2018).
28. Yang, S. *et al.* High-fidelity transfer and storage of photon states in a single nuclear spin. *Nature Photonics* **10**, 507–511 (2016).
29. Tsurumoto, K., Kuroiwa, R., Kano, H., Sekiguchi, Y. & Kosaka, H. Quantum teleportation-based state transfer of photon polarization into a carbon spin in diamond. *Communications Physics* **2**, (2019).
30. DiVincenzo, D. P. The Physical Implementation of Quantum Computation. *Fortschritte der Physik* **48**, 771–783 (2000).
31. Nagata, K., Kuramitani, K., Sekiguchi, Y. & Kosaka, H. Universal holonomic quantum gates over geometric spin qubits with polarised microwaves. *Nature Communications* **9**, 3227 (2018).
32. Sjöqvist, E. *et al.* Non-adiabatic holonomic quantum computation. *New Journal of Physics* **14**, 103035 (2012).
33. Togan, E. *et al.* Quantum entanglement between an optical photon and a solid-state spin qubit. *Nature* **466**,

- 730–734 (2010).
34. Vasconcelos, R. *et al.* Scalable spin–photon entanglement by time-to-polarization conversion. *npj Quantum Information* **6**, 9 (2020).
 35. Sekiguchi, Y. *et al.* Geometric entanglement of a photon and spin qubits in diamond. *Communications Physics* **4**, 264 (2021).
 36. Tycko, R., Pines, A. & Guckenheimer, J. Fixed point theory of iterative excitation schemes in NMR. *The Journal of Chemical Physics* **83**, 2775–2802 (1985).
 37. Khaneja, N., Reiss, T., Kehlet, C., Schulte-Herbrüggen, T. & Glaser, S. J. Optimal control of coupled spin dynamics: design of NMR pulse sequences by gradient ascent algorithms. *Journal of Magnetic Resonance* **172**, 296–305 (2005).
 38. Dolde, F. *et al.* High-fidelity spin entanglement using optimal control. *Nature Communications* **5**, 3371 (2014).
 39. Chen, Y. C. *et al.* Laser writing of coherent colour centres in diamond. *Nature Photonics* **11**, 77–80 (2017).
 40. Ruf, M. *et al.* Optically Coherent Nitrogen-Vacancy Centers in Micrometer-Thin Etched Diamond Membranes. *Nano Letters* **19**, 3987–3992 (2019).
 41. Yurgens, V. *et al.* Low-Charge-Noise Nitrogen-Vacancy Centers in Diamond Created Using Laser Writing with a Solid-Immersion Lens. *ACS Photonics* **8**, 1726–1734 (2021).
 42. Katona, G. *et al.* Fast two-photon in vivo imaging with three-dimensional random-access scanning in large tissue volumes. *Nature Methods* **9**, 201–208 (2012).
 43. Endres, M. *et al.* Atom-by-atom assembly of defect-free one-dimensional cold atom arrays. *Science* **354**, 1024–1027 (2016).
 44. Jiang, N. *et al.* Experimental realization of 105-qubit random access quantum memory. *npj Quantum Information* **5**, 28 (2019).